# Dual-modal metabolic analysis reveals hypothermia-reversible uncoupling of oxidative phosphorylation in neonatal brain hypoxia-ischemia

Naidi Sun[1,2,10,†], Yu-Yo Sun[3,4,5,†], Rui Cao[2], Hong-Ru Chen[4,5,6], Yiming Wang[2], Elizabeth Fugate[7], Marchelle R. Smucker[4,5], Yi-Min Kuo[8], P. Ellen Grant[9], Diana M. Lindquist[7], Chia-Yi Kuan[4,5,*], and Song Hu[1,*]

[1]Department of Biomedical Engineering, Washington University in St. Louis, St. Louis, MO 63130, USA
[2]Department of Biomedical Engineering, University of Virginia, Charlottesville, VA 22908, USA
[3]Institute of BioPharmaceutical Sciences, National Sun Yat-Sen University, Kaohsiung, Taiwan 80424, Taiwan
[4]Department of Neuroscience, University of Virginia, Charlottesville, VA 22908, USA
[5]Center for Brain Immunology and Glia (BIG), University of Virginia, Charlottesville, VA 22908, USA
[6]Department of Life Sciences and Institute of Genome Sciences, National Yang Ming Chiao Tung University, Taipei City, Taiwan 112304, Taiwan
[7]Department of Radiology, Cincinnati Children's Hospital Medical Center, Cincinnati, OH 45229, USA
[8]Department of Anesthesiology, Taipei Veterans General Hospital; Department of Anesthesiology, College of Medicine, National Yang Ming Chiao Tung University, Taipei City, Taiwan 11217, Taiwan
[9]Fetal-Neonatal Neuroimaging & Developmental Science Center, Boston Children's Hospital, Boston, MA 02115, USA
[10]Current address: Key Laboratory of Brain Health Intelligent Assessment and Intervention of the Ministry of Education, School of Medical Technology, Beijing Institute of Technology, Beijing 150081, China

[†]These authors contributed equally to this work.

[*]For correspondence: songhu@wustl.edu (Song Hu) or alex.kuan@virginia.edu (Chia-Yi Kuan)

**Additional information**

***Keywords:*** multi-parametric photoacoustic microscopy, cerebral oxygen metabolism, uncoupling of oxidative phosphorylation, neonatal brain hypoxia-ischemia, therapeutic hypothermia

***Funding:*** This work was supported by the National Science and Technology Council of Taiwan MOST 111-2320-B-110-003-MY2 (to Y.-Y.S.), NIH grants NS125788, NS135793, NS127392, and HD109025 (to C.-Y.K.), NS099261 and NS120481 (to S.H.), and NS125677 (to C.-Y.K. and S.H.), and NSF CAREER 202988 (to S.H.).

***Author contributions:*** S.H. and C.-Y.K. came up the research idea. D.M.L., P.E.G., S.H., and C.-Y.K. finalized the research plan and interpreted the experimental data. N.S., Y.-Y.S., R.C., H.-R.C., Y.W., E.F., M.R.S., and Y.-M.K. performed the experiment. S.H. and C.-Y.K. wrote the manuscript.

***Data availability:*** All data is included in the manuscript and/or supplementary files.

***Competing interest:*** The authors declare that no competing interests exist.

***Ethics:*** All procedures were approved by the Institutional Animal Care and Use Committees at the University of Virginia and Washington University in St. Louis.

**Abstract**

Hypoxia-ischemia (HI), which disrupts the oxygen supply-demand balance in the brain by impairing blood oxygen supply and the cerebral metabolic rate of oxygen ($CMRO_2$), is a leading cause of neonatal brain injury. However, it is unclear how post-HI hypothermia helps to restore the balance, as cooling reduces $CMRO_2$. Also, how transient HI leads to secondary energy failure (SEF) in neonatal brains remains elusive. Using photoacoustic microscopy, we examined the effects of HI on $CMRO_2$ in awake 10-day-old mice, supplemented by bioenergetic analysis of purified cortical mitochondria. Our results show that while HI suppresses ipsilateral $CMRO_2$, it sparks a prolonged $CMRO_2$-surge post-HI, associated with increased mitochondrial oxygen consumption, superoxide emission, and reduced mitochondrial membrane potential necessary for ATP synthesis—indicating oxidative phosphorylation (OXPHOS) uncoupling. Post-HI hypothermia prevents the $CMRO_2$-surge by constraining oxygen extraction fraction, reduces mitochondrial oxidative stress, and maintains ATP and N-acetylaspartate levels, resulting in attenuated infarction at 24 hours post-HI. Our findings suggest that OXPHOS-uncoupling induced by the post-HI $CMRO_2$-surge underlies SEF and blocking the surge is a key mechanism of hypothermia protection. Also, our study highlights the potential of optical $CMRO_2$-measurements for detecting neonatal HI brain injury and guiding the titration of therapeutic hypothermia at the bedside.

## Introduction

The human brain constitutes only 2% of the body mass, but utilizes ~20% of body's oxygen consumption (Rolfe and Brown, 1997). Disruptions in cerebral blood flow and oxygen supply cause a spectrum of brain injuries, including adult ischemic stroke and neonatal hypoxic-ischemic encephalopathy (HIE) (Allen and Brandon, 2011). In adult ischemic stroke, a >60% reduction in the cerebral metabolic rate of oxygen ($CMRO_2$) is indicative of looming infarction (Lee et al., 2003; Lin and Powers, 2018). However, the impacts of HIE on cerebral oxygen metabolism are far less certain due to the challenge of measuring $CMRO_2$ in infant brains by magnetic resonance imaging (MRI) or positron emission tomography (PET). Studies in animal models of HIE have revealed an initial recovery of brain adenosine triphosphate (ATP) levels during a short latent period after hypoxia-ischemia (HI), followed by a precipitous decline known as the secondary energy failure (SEF) that signifies looming infarction (Blumberg et al., 1997; Yager et al., 1992). However, the mechanisms of post-HI SEF and how therapeutic hypothermia protects neonatal brains against HI injury remain uncertain (Gunn et al., 2017). Also, it is unclear whether $CMRO_2$-measurments with recently developed bedside optical instruments, free of MRI's susceptibility to infant motion and PET's radiotoxicity, can detect HIE brain injury in a manner similar to adult ischemic stroke (De Carli et al., 2019; Dehaes et al., 2014; Ferradal et al., 2017; Jain et al., 2014).

Mitochondrial bioenergetics is vital to cellular functions and survival, and dysregulated oxidative-phosphorylation (OXPHOS) may promote neonatal HI brain injury (Niatsetskaya et al., 2012). While the phosphorylation efficiency of mitochondrial respiration (P/O ratio) remains stable over a wide range of substrate concentrations, it declines under hypoxia through a process known as OXPHOS-uncoupling (Kramer and Pearlstein, 1983), which is indicated by the rise of oxygen consumption despite a reduction of the mitochondrial membrane potential that is needed for ATP synthesis (Kristián and Siesjö, 1998). Although OXPHOS-uncoupling has been implicated in decoupling the contractive strength from oxidative metabolism after cardiac ischemia (Benzi and Lerch, 1992; Juhaszova et al., 2004), its role in HIE is unknown. We hypothesized that OXPHOS-uncoupling may be associated with mitochondrial injury in HIE, serving as the cause of post-HI SEF and a target for therapeutic hypothermia.

To test this hypothesis, we applied a head-restrained photoacoustic microscopy (PAM) technique to measure $CMRO_2$ during and immediately after HI in awake 10-day-old (P10) mice. Using

multi-parametric PAM, we simultaneously acquired high-resolution images of cerebral blood flow (CBF), the oxygen saturation of hemoglobin ($sO_2$), and the total concentration of hemoglobin ($C_{Hb}$), which can be combined to calculate $CMRO_2$ in absolute values (***Figure 1A*** and see **Methods** for details of the PAM system). The use of awake mouse neonates avoided the confounding effects of anesthesia on CBF and $CMRO_2$ (Cao et al., 2017; Gao et al., 2017; Sciortino et al., 2021; Slupe and Kirsch, 2018). In addition, we measured the oxygen consumption rate (OCR), reactive oxygen species (ROS), and the membrane potential of mitochondria that were immediately purified from the same cortical area imaged by PAM. This dual-modal analysis enabled a direct comparison of cerebral oxygen metabolism and cortical mitochondrial respiration in the same animal. Moreover, we compared the effects of therapeutic hypothermia on oxygen metabolism and mitochondrial respiration, and correlated the extent of $CMRO_2$-reduction with the severity of infarction at 24 hours after HI. Our results suggest that blocking HI-induced OXPHOS-uncoupling is an acute effect of hypothermia and that optical detection of $CMRO_2$ may have clinical applications in HIE.

## Results

### *Effects of Cooling and Hypoxia on $CMRO_2$ in Uninjured Mouse Neonates*

First, we studied the effects of hypothermia alone on neonatal $CMRO_2$. As shown in ***Figure 1A and B***, an awake P10 mouse was placed between the PAM apparatus and a water-floated voluntary treadmill, with the temperature of the water tank above the mouse head adjusted to achieve normothermia or hypothermia based on the skull temperature (***Figure S1***). Note that while the mouse skull was exposed, no craniotomy was necessary. Multi-parametric PAM images over a 5 × 3 $mm^2$ region from the Bregma to Lambda in both cortices were acquired within 40 minutes (***Figure 1C***). Using this system, we assessed the effects of hypothermia (from 37 °C to 32 °C to 29 °C of the mouse skull temperature) on $CMRO_2$ in uninjured mice (***Figure 1D***). Quantitative analysis revealed a decline in CBF from 38.37 mL/100g/min at 37 °C to 33.18 mL/100g/min at 32 °C (86% of the baseline) and to 22.65 mL/100g/min at 29 °C (59% of the baseline) (***Figure 1E***, left). In contrast, OEF remained unchanged at 32 °C and slightly declined to 85% of the baseline at 29 °C (***Figure 1E***, middle). Consequently, $CMRO_2$ declined from 2.27 mL/100g/min at 37 °C to 1.97 mL/100g/min at 32 °C (86% of the baseline) and further to 1.13 mL/100g/min at 29 °C (50% of the baseline) (***Figure 1E***, right). These results show that

hypothermia reduces $CMRO_2$ in uninjured mouse neonates, primarily through the suppression of CBF.

Next, we studied the effects of hypoxia alone on neonatal $CMRO_2$. Exposing anesthetized P10 mice to hypoxia (10% $O_2$) resulted in an increase of $CMRO_2$ (from 0.91 to 1.51 mL/100g/min), which was attributed to the rise in both CBF (from 24.04 to 30.74 mL/100g/min) and OEF (from 0.17 to 0.29) (***Figure 1F and G***). While this observation of greater oxygen consumption under a lower oxygen tension is seemingly counterintuitive, it aligns with the previous reports of higher $CMRO_2$ and cytochrome c oxidase (CCO) activity in mild hypoxia (Tsuji et al., 1995; Vestergaard et al., 2016). This phenomenon is presumably due to an increased cerebral energy demand under hypoxia.

***Effects of Combined HI on $CMRO_2$ and Mitochondrial Respiration***

Then, we studied the effects of combined HI under the Vannucci model, which involves unilateral common carotid artery (CCA) occlusion and transient hypoxia (Kuan et al., 2021; Yang et al., 2009). Using time-lapse PAM, we compared the dynamic changes of CBF, OEF, and $CMRO_2$ in the two hemicortices from unilateral CCA-ligation to combined HI (40 minutes), and for 2 hours upon returning to normoxia in awake P10 mice (***Figure 2A–D*** and ***Table S1***).

Before the onset of hypoxia, CCA-ligation alone did not provoke a significant difference in $CMRO_2$ between the two hemicortices (1.56 *vs.* 1.26 mL/100g/min; *p*-value, 0.6107; the first pair of red and green points in ***Figure 2D***). When hypoxia was initiated, however, the contralateral (CL) cortex had a significant increase in $CMRO_2$, similar to the responses in uninjured mice, while the CCA-ligated counterpart showed a marked reduction in $CMRO_2$ (0.78 *vs.* 2.37 mL/100g/min; *p*-value, 0.0011; the second pair of red and green points in ***Figure 2D***). Upon switching back to normoxia, $CMRO_2$ in the CL cortex quickly returned to the pre-hypoxia level and rose slowly afterwards, while $CMRO_2$ in the ipsilateral (IL) cortex rapidly rebounded above the pre-hypoxia level and remained elevated for at least 2 hours (the last three red and green points in ***Figure 2D***).

To determine the causes of the post-HI $CMRO_2$-surge, we recorded electroencephalography (EEG) of the P10 mouse before, during, and after HI to test whether the surge was due to status

epilepticus (Lin and Powers, 2018). Although showing seizure-like behaviors and a few spike-wave discharges on top of the EEG-suppression during HI (***Figure 2E***, hypoxia), mice only showed a gradual recovery from the suppression without burst discharges on EEG post-HI (***Figure 2E***, normoxia). Thus, the post-HI $CMRO_2$-surge was not attributed to status epilepticus.

We then isolated the mitochondria from both hemicortices of injured mouse brains at 2 or 5 hours post-HI and from the uninjured (UN) mouse brains for *in-vitro* analysis (see **Materials and Methods** for details of the mitochondrial function analysis). At 2 hours post-HI, mitochondria from the IL cortex showed increased OCR (***Figure 2F*** and ***Figure S2***) and superoxide (as measured by the MitoSox Red fluorescence, ***Figure 2G***), but reduced mitochondrial membrane potential ($\psi_m$, as measured by the ΔRH-123 fluorescence, ***Figure 2H***), compared to mitochondria in the CL cortex or the UN brain. By 5 hours post-HI, mitochondria in the IL cortex manifested a lower OCR and $\psi_m$, but an even higher superoxide emission, suggesting more substantial mitochondria injury (***Figure 2F–H***). In contrast, mitochondria in the CL cortex at both 2 and 5 hours post-HI showed comparable OCR, superoxide, and $\psi_m$ to those from the UN brain (***Figure 2F–H***). These results suggest that post-HI $CMRO_2$-surge can be attributed to OXPHOS-uncoupling and ROS-emission, which may promote mitochondrial injury.

***Effects of Hypothermia Treatment on HI-induced $CMRO_2$ Surge and Mitochondria Injury***

Next, we tested the effects of therapeutic hypothermia on $CMRO_2$ and mitochondrial functions. To mimic clinical settings, CCA-ligation and combined HI were performed at the room temperature, while hypothermia was initiated after HI by reducing the mouse skull temperature from 37 °C to 32 °C (***Figure 3A–D***).

Similar to ***Figure 2D***, HI provoked a rise of $CMRO_2$ in the CL cortex and a decline of $CMRO_2$ in the IL cortex (***Figure 3D***). Notably, post-HI hypothermia blunted the $CMRO_2$-surge in the IL cortex, locking it at the pre-HI level throughout the 2-hour monitoring period (***Figure 3D*** and ***Table S2***). Comparison of the PAM measurements obtained under normothermia *vs.* hypothermia revealed that the chief effect of hypothermia was to block the rise of post-HI OEF rather than reducing CBF (***Figure 3E***), as observed in the uninjured neonates (***Figure 1E***). Similar to our results, a recent study also showed minimal reduction of post-HI CBF by hypothermia at 32 °C (Buckley et al., 2015).

We then tested whether therapeutic hypothermia protects mitochondria and prevents the onset of SEF, as previously postulated (Gunn et al., 2017). We isolated mitochondria from the CL and IL cortex, with or without the 4-hour hypothermia treatment for *in-vitro* analysis at 5 hours post-HI (i.e., 1 hour after the conclusion of the hypothermia treatment). As shown in ***Figure 3F–I***, mitochondria isolated from the IL cortex without hypothermia treatment showed reduced OCR, higher superoxide, as well as lower hydrogen peroxide ($H_2O_2$) and mitochondria $\psi_m$, compared to those receiving hypothermia treatment or from the CL cortex. In contrast, mild hypothermia (32 °C) had no suppressive effects on OCR, superoxide and $H_2O_2$ emission, and $\psi_m$ of mitochondria in the CL cortex. We also compared the mitochondrial ATP levels at 6 hours post-HI and found a higher ATP level (0.64 μmol/g) in the IL cortex receiving hypothermia treatment than those without hypothermia (0.33 μmol/g, ***Figure 3J***). These results confirmed that therapeutic hypothermia maintained mitochondrial OCR and $\psi_m$, reduced superoxide and $H_2O_2$ emission, and prevents post-HI SEF.

***Using Optically Measured $CMRO_2$ to Detect Neonatal HI Brain Injury***

Finally, we compared $CMRO_2$ and brain infarction with or without hypothermia treatment at 24 hours after HI. PAM measurements (***Figure 4A***) and tissue-level $CMRO_2$ mapping (***Figure 4B***) showed better preservation of oxygen metabolism in the IL cortex of hypothermia-treated mice, compared with those without the treatment. Notably, the marked reduction of $CMRO_2$ at 24 hours post-HI in non-treated mice (***Figure 4B***) was coupled to impaired triphenyl-tetrazolium chloride (TTC) staining, which corresponded to tissue infarction (***Figure 4C***). The TTC analysis confirmed the reduction of infarct size in mice receiving therapeutic hypothermia than those without (8.74 $mm^3$ *vs.* 45.25 $mm^3$, ***Figure 4D***). Direct comparison of the hemodynamic and oxygen-metabolic parameters showed that post-HI hypothermia maintained CBF (41.13 mL/100g/min), OEF (0.23), and $CMRO_2$ (2.12 mL/100g/min) in the IL cortex to a level similar to those in the CL cortex (blue bars in ***Figure 4E–G***). In contrast, mice without hypothermia treatment showed a marked reduction of OEF (0.04) and $CMRO_2$ (0.35 mL/100g/min) in the IL cortex at 24 hours post-HI (gray bars in ***Figure 4E–G***).

Additionally, the proton nuclear magnetic resonance (NMR) analysis showed significant reductions of total creatine (Cr/PCr), choline (Cho), glutamate and glutamine (Glx), and NAA in

the IL cortex, compared to those in the CL cortex, in mice without hypothermia treatment (***Figure 4H*** and gray bars in ***Figure S3***). In contrast, mice that received therapeutic hypothermia maintained similar levels of Cr/PCr, Cho, and NAA between the two hemicortices (***Figure 4I*** and light blue bars in ***Figure S3***). These results suggest that marked reduction of post-HI $CMRO_2$ signifies SEF and tissue infarction, similar to that in adult ischemic stroke (Lee et al., 2003; Lin and Powers, 2018).

**Discussion**

Acute post-asphyxia HIE around the time of birth remains a major cause of neonatal death and lifelong neurological deficits. Clinical observations and animal studies suggest that brain cells initially recover from the insult during a short latent phase, typically lasting ~6 hours, but then enter a deterioration phase characterized by progressive failure of oxygen metabolism (i.e., SEF), seizures, and death (Blumberg et al., 1997; Gunn et al., 2017; Yager et al., 1992). Acute treatment with mild hypothermia (32–34 °C) prevents the onset of SEF in moderate HIE, but the mechanisms remain unclear for at least two reasons (Gunn et al., 2017). First, hypothermia normally inhibits instead of enhancing cerebral oxygen metabolism. Second, since mild hypothermia has little effect on the EEG activity (Erecinska et al., 2003), which does not support the common notion that it protects through suppression of neuronal activity and cerebral energy demand. In this study we combined PAM-based optical measurement of $CMRO_2$ and functional assays of acutely purified cortical mitochondria in HI-injured awake mouse neonates to investigate the causes of post-HI SEF and hypothermia protection. Our study has three unique features. First, awake-brain imaging avoids the confounding effects of anesthesia on CBF and $CMRO_2$ (Cao et al., 2017; Gao et al., 2017; Sciortino et al., 2021; Slupe and Kirsch, 2018). Second, our PAM-based $CMRO_2$-measurement is analogous to optical $CMRO_2$-detection using bedside instruments that may enable non-invasive monitoring of neonatal brain injury (De Carli et al., 2019; Dehaes et al., 2014; Ferradal et al., 2017; Jain et al., 2014; Liu et al., 2014a). Third, our experiments establish a direct connection between the impacts of HI on $CMRO_2$ and that on mitochondria, which account for the majority of cerebral oxygen metabolism (Rolfe and Brown, 1997). In the following, we discuss the implications of our findings on the cause of post-HI SEF, the protective mechanisms of hypothermia in HI, and the potential of optic $CMRO_2$-detection in neonatal care.

***Causes of post-HI SEF: uncoupled OXPHOS and excessive ROS***

In normal conditions, $CMRO_2$ remains relatively stable over a range of CBF and brain glucose-uptake changes as the so-called "uncoupling of CBF and cerebral oxygen metabolism" (Fox and Raichle, 1986). The autoregulation of $CMRO_2$, accomplished by alterations of OEF (an index of oxygen diffusion across capillaries) in the opposite direction of CBF fluctuations, maintains a consistent level of mitochondrial respiration, while glycolysis and phosphocreatine-creatine conversion support the transient outbursts of neural activity (Chen et al., 2022; Lin and Powers, 2018).

As illustrated by our PAM measurements in unilateral CCA-ligation, the IL cortex showed OEF-elevation to compensate for a lower CBF than the CL cortex and maintained bilaterally similar $CMRO_2$ values (***Figure 2D*** and ***3D***, and ***Table S1*** and ***S2***). During combined HI, the CL cortex showed up-regulation of both CBF and OEF and produced a higher $CMRO_2$, similar to the responses to moderate hypoxia (10% $O_2$) in uninjured animals (***Figure 1G***). These responses suggest a greater demand of brain energy as adaptation to hypoxia. In contrast, the IL cortex showed a smaller increase of CBF and mild or no changes of OEF in combined HI, leading to a 40–50% reduction in $CMRO_2$ (***Figure 2D*** and ***3D***, and ***Table S1*** and ***S2***). Consistent with our findings, previous studies showed marked reduction of ATP and phosphocreatine, as well as a massive buildup of lactate, in the IL cortex during combined HI, while the CL cortex showed only minimal ATP-reduction and modest accumulation of lactate (Chen et al., 2022; Gunn et al., 1997; Salford and Siesjö, 1974). The bilateral disparity of ATP homeostasis-versus-reduction during combined HI may influence the divergent $CMRO_2$ responses post-HI: the CL cortex showed $CMRO_2$ recovery to the pre-HI level because extra ATP-output is no longer required to cope with hypoxia, while the IL cortex developed a surge of mitochondrial respiration (and thus $CMRO_2$) presumably to recompense the energy deficit incurred during HI (***Figure 2D and 2F***).

Persistent increase in oxygen consumption, albeit to a lesser degree, was also observed in post-ischemic myocardium and after spreading depression in rodent cerebral cortex (Benzi and Lerch, 1992; Juhaszova et al., 2004; Piilgaard and Lauritzen, 2009). Moreover, brain-injured infants showed a higher $CMRO_2$ than healthy neonates (Grant et al., 2009), suggesting that the rebound of oxygen metabolism is a generic response to transient severe HI. Notably, our PAM

measurements showed that the rise of post-HI $CMRO_2$ is primarily driven by the increase of OEF (***Figure 2C*** and ***Table S1***), which may be due to reduction of capillary transient time heterogeneity (Paulson et al., 2010). The HI-induced energy deficit and tissue hypoxia may also assist oxygen diffusion across capillaries to elevate the OEF (Chen et al., 2022; Salford and Siesjö, 1974; Yang et al., 2009). Finally, post-HI acidosis may also promote mitochondrial respiration (Jespersen and Østergaard, 2012; Khacho et al., 2014). We suggest that these cellular and vascular factors collectively promote mitochondrial respiration and $CMRO_2$ immediately after HI (***Figure 5A***).

However, the post-HI mitochondrial respiration has features of OXPHOS uncoupling and ROS release, as shown by the rise of oxygen consumption and mitochondrial superoxide despite the reduction of mitochondrial membrane potential needed for ATP-synthesis through F0/F1 ATPase (***Figure 2F–H***). The triggers of OXPHOS uncoupling after HI may include persistent tissue hypoxia (Kramer and Pearlstein, 1983; Kuan et al., 2021), influx of calcium in the mitochondrial matrix (Benzi and Lerch, 1992; Kristián and Siesjö, 1998), reverse electron transfer through Complex I (Kim et al., 2018), nitric oxide-mediated inhibition of the cytochrome oxidase in Complex IV (Cooper and Giulivi, 2007), and ROS-caused disruption of the electron transport chain super-complexes and mitochondrial cristae (Paradies et al., 2018), according to the literature and our results (***Figure S4***). Importantly, the release of extra ROS during uncoupled OXPHOS injures the mitochondria (Granger and Kvietys, 2015; Murphy, 2009), as indicated by the reduction of oxygen consumption and mitochondrial membrane potential at 5 hours post-HI, if without hypothermia treatment (***Figure 2F–H***). These results suggest that uncoupled OXPHOS and ROS-mediated injury of mitochondria are important mechanisms of post-HI SEF (***Figure 5A***).

***Protective mechanisms of hypothermia***

If the aforementioned hypothesis is correct, therapeutic hypothermia shall attenuate the post-HI $CMRO_2$-surge. Indeed, our data showed that the initiation of mild hypothermia (32 °C) post-HI efficiently clamped the rebounding $CMRO_2$ to the pre-HI level at both hemicortices over the 2-hour PAM-monitoring period (***Figure 3D***). Furthermore, hypothermia blocked the rapid demise of mitochondria at 5 hours post-HI (***Figure 3F–I***) and preserved cortical ATPs at 6 hours post-HI (***Figure 3J***). In other words, neonatal mice recovering under mild hypothermia after HI escaped

the initial overshoot of $CMRO_2$ and the subsequent SEF, as predicted by our hypothesis (***Figure 5A***).

In terms of mechanism, our PAM measurements showed that hypothermia mainly blocks the rise of post-HI OEF to constrain $CMRO_2$ (***Figure 3E*** and ***Table S2***). This is different from the responses to mild hypothermia (32 °C) in uninjured mice, which showed CBF-reduction but negligible changes in OEF (***Figure 1E***). This difference suggests unique effects of hypothermia in the post-HI brain. Previous studies showed that mild hypothermia represses glycolysis and the tricarboxylic acid (TCA) cycle at the phosphofructokinase and isocitrate dehydrogenase step, respectively (Berntman et al., 1981; Hägerdal et al., 1975). Consequently, the buildup of lactate and acidosis and the electron transport chain reactions in OXPHOS are attenuated, which may repress post-HI mitochondrial respiration and prevent SEF and brain injury according to our hypothesis (***Figure 5B***).

Whether hypothermia reduces post-HI brain glucose-uptake, however, remains unclear. Although previous studies showed a reverse correlation of cerebral glucose metabolism (CMRglu) and the severity of HIE in neonates at 4–24 days of age (Thorngren-Jerneck et al., 2001), the responses of CMRglu in the acute post-HI phase remain unknown. If post-HI CMRglu is similarly up-regulated due to energy deficit, the influx of glucose and the ensuing glycolysis may stimulate mitochondrial respiration to produce greater ROS injury, while hypothermia typically represses CMRglu and could reduce HI injury in this scenario (Erecinska et al., 2003). Future studies are thus warranted to examine the impacts of HI with or without hypothermia treatment on CMRglu in mouse neonates.

***Optical $CMRO_2$ detection in neonatal care***

Early detection of brain injury in neonatal care has profound importance for early intervention, treatment optimization, and outcome prognostication. Although MRI is the gold standard for detecting acute brain injury, its application in early diagnosis and HIE therapy is hampered by non-portability, high cost, and susceptibility to motion. In contrast, advances in combined near infrared spectroscopy (NIRS) and diffuse correlation spectroscopy (DCS) have enabled optical $CMRO_2$ detection as a non-invasive, bedside procedure in neonatal care (De Carli et al., 2019; Dehaes et al., 2014; Ferradal et al., 2017; Jain et al., 2014; Liu et al., 2014a). This is owing to the

relatively thin infant skull compared to that of adults and the separation of anterior and posterior fontanelle sutures, which facilitate the penetration of infrared light to quantify the brain tissue oxygenation. The combination of NIRS-based cerebral oximetry and DCS-based CBF mapping in the same area enables quantitative measurements of the regional $CMRO_2$ index or $CMRO_{2i}$. The NIRS/DCS-measured $CMRO_{2i}$ correlates well with the MRI-measured $CMRO_2$ in neonates and declines during hypothermic cardiopulmonary bypass (Dehaes et al., 2014; Ferradal et al., 2017; Jain et al., 2014). A phase 1 clinical trial (NCT02815618) is underway to determine the safety of NIRS/DCS and the normal $CMRO_{2i}$ in newborn infants (De Carli et al., 2019). Notably, our PAM technique is analogous to NIR/DCS, and both methods measure $CMRO_2$ in the cortical layers. Moreover, a past NIR/DCS study suggested increased cerebral oxygen consumption in infants with HIE symptoms (Grant et al., 2009), which echoes our findings. Thus, our results may shed insights into the utility of optical $CMRO_2$ detection in neonatal care.

In adult ischemic stroke patients, $CMRO_2$ can be used to differentiate the infarct core and the adjacent penumbra area, where brain cells are energy-strained but remain salvageable if local blood oxygen supply is restored promptly (Lin and Powers, 2018). The cut-off for "salvageable penumbra" is usually at <60% reduction of $CMRO_2$ (Lee et al., 2003). Our results showed that HI-injured mouse neonates preserved 85% of $CMRO_2$ at 24 hours post-HI if recovered under mild hypothermia (32 °C), but lost ~75% of $CMRO_2$ without this treatment (***Figure 4G***). Further, the severity of $CMRO_2$-reduction at 24 hours correlate with infarction, as shown by the results of TTC-stain immediately after PAM-imaging (***Figure 4B and C***). These results suggest that a minimal level of $CMRO_2$ to prevent infarction may also exist in infants after HI, as in adults after ischemic stroke, despite that the normal $CMRO_2$ in infants is lower than that in adults and may differ between term and preterm neonates (Altman et al., 1993; Liu et al., 2014b). Since NIRS/DCS-based $CMRO_{2i}$ measurement is a non-invasive procedure, it can be performed repeatedly to detect early brain injury through the trajectory of $CMRO_{2i}$ alterations in neonates with clinical HIE symptoms.

## Methods

### *Multi-parametric PAM System*

As shown in ***Figure 1A***, a nanosecond-pulsed laser (wavelength: 532 nm, repetition rate: up to 30 kHz; BX40-2-G, EdgeWave) was used in the PAM system for imaging the neonatal mouse brain.

The laser beam firstly passed through a half-wave plate (HWP; WPH05M-532, Thorlabs) and an electro-optical modulator (EOM; 350-80, Conoptics) for precise control of the polarization state of the incident beam. By alteration of the voltage applied to the EOM, the polarization state could be dynamically switched between the vertical direction and the horizontal direction, which allowed a polarizing beam splitter (PBS; PBS121, Thorlabs) to dispatch the laser pulses between two optical paths through either reflection or transmission. In the reflection path, after being partially attenuated by a neutral-density filter (NDF; NDC-50C-2M, Thorlabs), the beam was coupled through a fiber collimator (CFC-11X-A, Thorlabs) into a polarization-maintaining single-mode fiber (PM-SMF; F-SPA, Newport) for stimulated Raman scattering-based wavelength conversion. The output of the PM-SMF was collimated by an identical collimator and purified by a bandpass filter (BPF; FB560-10, Thorlabs) to isolate the 558-nm component. Then, the 558-nm Raman beam generated in the reflection path and the 532-nm beam in the transmission path were combined by a dichroic mirror (DBS; FF538-FDi01, Semrock) and coupled into a single-mode fiber (SMF; P1-460B-FC-2, Thorlabs) through a fiber collimator (CFC-11X-A, Thorlabs), before which ~5% of the combined beam was picked off by a beam sampler (BS; BSF10-A, Thorlabs) and monitored by a high-speed photodiode (PD; FDS100, Thorlabs) to compensate for possible fluctuation in the laser energy. The dual-wavelength laser beam was then delivered to the scanning head, where two identical doublets (DL; AC127-025-A, Thorlabs) were used to map the fiber output into the tissue to be imaged, and a correction lens (CL; LA1207-A, Thorlabs) was used to compensate for the optical aberration at the air-water interface. A ring-shaped ultrasonic transducer (UT; inner diameter: 2.2 mm; outer diameter: 4.0 mm; center frequency: 35 MHz; 6-dB bandwidth: 70%) was used for confocal alignment of the optical excitation and ultrasonic detection. A customized water tank (WT) was used to immerse the ultrasonic transducer for acoustic coupling. As shown in ***Figure 1B***, the mouse head was fixed to a customized metal arm-piece through a wearable 3-D printed head plate for head-restrained awake-brain imaging. A water-floated treadmill (03170-1008, Blick Art Materials) was used to allow the mouse to move freely with reduced reaction force (Cao et al., 2017). A gas inlet and a customized face mask from syringe were used to deliver the inhalation gas (*i.e.,* normoxia or hypoxia).

***Procedures for PAM Imaging***

Before imaging of the neonatal mouse brain, the animal was first anesthetized with vaporized isoflurane (EZ-SA800, E-Z Systems) for installation of the head-restraint plastic head plate (Sciortino et al., 2021). Hair on the mouse scalp was removed by a trimmer (9990-1301, Wahl Clipper), and then the scalp was removed with surgical scissors (MDS10030, Medline Industries) to expose the skull. After the clearance of the blood, debris, and remaining hairs, the gel-based cyanoacrylate glue (234790, Loctite) was applied to all edges of the head plate, which was attached to the center of the skull between the Bregma and Lambda. After the applied glue is solidified (~20 min), the frame-worn animal was carefully moved to the treadmill and secured to the metal arm-piece with two #4–40 screws. Throughout the frame installation, the body temperature of the mouse was maintained at 37 °C using a homeothermic monitoring system (No. 69020, RWD life science).

After the installation of the head-restraint head plate, a thin layer (~1 mm) of ultrasound gel (Aquasonic CLEAR®, Parker Laboratories) was applied to the surface of the skull for effective acoustic coupling. Then, the metal arm-piece and the treadmill were carefully raised to bring the gel in gentle contact with the bottom of the water tank, which was filled with temperature-maintained deionized water. After fully recovering from the anesthesia, the neonatal mouse was ready for awake-brain imaging by the multi-parametric PAM system, which was controlled by a field-programmable gate array (PCIe-7841R, National Instruments) through a self-developed LabVIEW program. For the imaging field covering both hemicortices between the Bregma and Lambda of the neonatal mouse ($5 \times 3$ mm$^2$ as shown in ***Figure 1C***), the acquisition time is ~40 minutes with step sizes set to 0.1 and 10 µm along the *x*- and *y*-direction, respectively.

***PAM Imaging under Normothermia or Hypothermia***

The temperature of the water tank was controlled by a temperature controller (EW-89802-52, Cole-Parmer), which could also be used to effectively regulate the temperature of the underlying mouse skull. Based on our calibration experiment (***Figure S1***), the normothermia condition (37 °C) could be achieved with the water temperature set to 39 °C; while for the two hypothermia conditions (32 °C or 29 °C), the water temperature was set to 33 °C or 29 °C, respectively. Throughout all the experiments, the skull temperature was closely monitored by a thin-film temperature sensor (F3132, Omega) attached to the skull. Note that the PAM measurements were

performed one hour after each temperature adjustment to ensure equilibrium under the new temperature setting.

***PAM Imaging under Normoxia or Hypoxia***

For normoxia, the oxygen concentration in the inhalation gas was 21% (AI M-T, Praxair). For hypoxia, the medical-grade air was mixed with medical-grade nitrogen gas (NI-H, Praxair) through a gas flowmeter mixer (EW-03218-56, Cole-Parmer) to achieve a reduced oxygen concentration of 10%, which was confirmed by a clinical anesthesia monitor (Capnomac Ultima, Datex-Ohmeda). Under both conditions, the flow rate of the inhalation gas was set to 1.5 L/min.

***PAM Imaging of the Vannucci HI Model***

In the Vannucci HI study, the first PAM image set was acquired at 37 °C after the unilateral CCA ligation. Then, the second image set was acquired at 37 °C during the one-hour HI challenge. Subsequently, three sequential image sets were acquired up to 120 minutes (*i.e.,* 0–40, 40–80, and 80–120 minutes) post-HI, either under normothermia (37 °C) or hypothermia (32 °C) by regulating the temperature of the water tank.

***Quantification of Cerebral Hemodynamics and Oxygen Metabolism by PAM***

Our PAM technique enables simultaneous quantification of multiple microvascular parameters, including $C_{Hb}$, $sO_2$, and blood flow by the statistical, spectroscopic, and correlation analyses of the acquired A-line signals, respectively (Cao et al., 2017). With our self-developed MATLAB-based vessel segmentation algorithm (Sun et al., 2020), these hemodynamic parameters could be extracted at the single-microvessel level. Then, CBF, OEF, and $CMRO_2$ could be obtained by the following formulas:

$$CBF = \pi v d^2/8$$

$$OEF = (s_aO_2 - s_vO_2)/s_aO_2$$

$$CMRO_2 = \xi \times C_{Hb} \times s_aO_2 \times OEF \times CBF$$

where $d$ is the vascular diameter, $v$ is the peak flow speed along the vascular axis, $s_aO_2$ and $s_vO_2$ are the $sO_2$ values of the feeding arteries and draining veins, respectively (Cao et al., 2017), and $\xi$ is the oxygen binding capacity of hemoglobin (0.014 L $O_2$ per gram hemoglobin).

***Neonatal Cerebral HI and Hypothermia Treatment***

The Vannucci model of neonatal HI with and without hypothermia treatment was performed in P10 C57BL/6 mice as described (Chen et al., 2021; Kuan et al., 2021; Yang et al., 2009). Briefly, P10 mice of both sexes anesthetized with 2% isoflurane were subjected to the right CCA-ligation. After a recovery period for one hour, mice were exposed to 10% $O_2$ for 40 minutes in a hypoxic chamber at 37 °C. The mice were recovered to normoxia (21% $O_2$) condition, and then randomly divided into normothermia or hypothermia groups with the chambers submerged in a 37 °C or 32 °C water bath, separately for a total four-hour treatment. The body temperature of mice was monitored at 37 °C or 32 °C using a rectal probe (BAT-12 microprobe, Physitemp) during the treatment.

***Measurement of Brain Infarction***

Detection of brain infarction was performed by TTC staining (Sigma-Aldrich) at 24 hours post-HI as previously described (Kuan et al., 2021; Yang et al., 2009). The fresh brains were collected after cold-PBS transcardial perfusion. The whole brain (***Figure 4C***) or 1 mm-thick brain sections (***Figure 4D***) were incubated with 2% TTC solution, and the TTC-unstained volume in all sections were quantified using the NIH ImageJ software.

***HR-MAS NMR Study***

The *ex-vivo* NMR experiments and analyses of mice brain tissues were performed as previously reported (Chen et al., 2021). Briefly, a 1.5-mm punch (~10 mg) was taken from snap-frozen brain tissue and loaded into a sample rotor (4 mm $ZrO_2$, Bruker Instruments), with 4 μL of deuterium oxide containing 100 mM sodium trimethylsilylpropionate-d4 (TSP, Sigma-Aldrich) added to obtain a frequency-lock signal and serve as an internal standard for chemical shift. HR-MAS NMR experiments were then carried out on an NMR spectrometer (AVANCE 400 WB, Bruker) with a dedicated 4 mm HR-MAS probe. Spinning rate of samples was set to 2500 kHz (± 2 Hz) at 4 °C. A T2-weighted, water-suppressed Carr-Purcell-Meiboom-Gill pulse sequence was used to acquire the data. The $^1$H-NMR spectra were recorded using key parameters as follows: repetition time of 2.0 seconds, spectral width of 4.8 kHz, 32K data points, and 256 transients. The presence and concentrations of selected metabolites in brain tissue samples were determined based on their chemical shifts and corresponding integrals using the Electronic REference To access In vivo Concentration (ERETIC) reference method (Bruker), with 10 mM TSP as the external standard.

***ATP Detection***

The brain ATP level was measured through an ATP Assay Kit (Catalog No. ab83355, Abcam) according to the manufacturer's instructions. Briefly, mouse brains were harvested, washed with 1X PBS, and then resuspended in 100 µL of ATP assay buffer. Cells were homogenized and then centrifuged at 4 °C at 12,000 g to remove the insoluble material. The supernatants were collected and incubated with the ATP probe. Absorbance was detected at 580 nm using a microplate reader (SpectraMax® M3 Microplate Reader, Molecular Devices).

***Assessment of Isolated Brain Mitochondrial Function***

Mitochondria were isolated from the brain tissues using Percoll density gradient centrifugation as described before (Caspersen et al., 2008; Niatsetskaya et al., 2012). Mitochondrial respiration was measured by a Clark-type electrode (Oxytherm, Hansatech). Briefly, 0.05 mg mitochondria protein were added into 0.5 mL respiration buffer at pH 7.2, which consists of 200 mM sucrose, 25 mM KCl, 2 mM $K_2HPO_4$, 5 mM HEPES, 5 mM $MgCl_2$, 0.2 mg/mL of BSA, 30 µM $P^1$, $P^5$-di(adenosine 5')-pentaphosphate (Ap5A), 10 mM glutamate, and 5 mM malate at 32°C, with the addition of 5 mM succinate to trigger respiration. As shown in ***Figure S2***, to initiate State 3 phosphorylating respiration, 100 nmol of adenosine diphosphate (ADP) was added to the mitochondrial suspension.

The rate of $O_2$ consumption was presented in nmol $O_2$/mg mitochondrial protein/min. The respiratory control ratio was calculated as the ratio of the State 3 respiration rate versus the State 4 resting respiration rate recorded after the phosphorylation of ADP has been finished. 35 nM 2'-4' Dinitrophenol (DNP) was used to initiate uncoupled respiration (Kim et al., 2018).

The rate of $H_2O_2$ emission from isolated mitochondria was measured using a fluorescence assay by a fluorescence spectrophotometer (F-7000, Hitachi High Technologies America, Inc), which was set at 555-nm excitation and 581-nm emission as previous study (Starkov and Fiskum, 2003). Briefly, 0.05 mg mitochondria were added into 1 mL respiration buffer and supplemented with 5 mM succinate, 10 µM Amplex Ultrared (Catalog No. A22180, Invitrogen), and 4 U/mL horse radish peroxidase (HRP). After recording the fluorescence for 400 seconds, samples were added with 1 µM rotenone, then added with 1µg/mL antimycin A after another 200 seconds. The

calibration curve was calculated by sequential additions of known amounts of $H_2O_2$, with the cuvette containing the respiration buffer, Amplex Ultrared, and HRP.

Superoxide was monitored with MitoSOX Red (Catalog No. M36008, Invitrogen). Briefly, 5 µM MitoSOX Red was added to the cuvettes and the fluorescence was measured at 510-nm excitation and 579-nm emission wavelengths. Time-dependent monitoring of the MitoSOX Red-related fluorescence was done using a fluorescence spectrophotometer (F-7000, Hitachi High Technologies America, Inc) at 25 °C. Since a saturation of kinetics established after 25 minutes of the recording, the initial linear increase rates of the MitoSOX Red-related fluorescence were used for quantification.

For membrane potential analysis, the rhodamine 123 (RH-123; Sigma-Aldrich) quenching technique was conducted. 0.05 mg isolated mitochondria were incubated with 0.3 mM RH-123 and analyzed by a fluorescence spectrophotometer (F-7000, Hitachi High Technologies America, Inc), using excitation and emission wavelengths of 503 nm and 527 nm, respectively. During the measurements, the reaction buffer containing mitochondria was continuously stirred. Baseline fluorescence was recorded for 300 seconds followed by the sequential addition of oxidizable substrates (7 mM succinate or 7 mM malate and glutamate) and 50 mM carbonyl cyanide m-chlorophenyl hydrazone (CCCP).

***Video-EEG Monitoring***

Video-EEG monitoring of mouse neonates was performed as described (Burnsed et al., 2019). Briefly, nine-day-old (P9) C57BL/6 mice had unipolar insulated stainless steel depth electrodes (bare diameter: 0.005 inch, coated: 0.008 inch; A-M Systems, Sequim) stereotactically implanted in the bilateral parietal cortices (−1.2 dorsoventral (DV), ±0.5 mediolateral (ML), and −1.0 deep (D) mm), bilateral CA1 region of the hippocampus (−3.5 DV, ±2.0 ML, and −1.75 D mm), and a reference electrode in the cerebellum. Following recovery, mice were exposed to HI on P10. A unity gain impedance matching head stage (TLC2274 Quad Low-Noise Rail-to Rail Operational Amplifier, Texas Instruments) was used for recordings, which began 1 hour prior to CCA ligation and continued through 2 hours after re-oxygenation post-ligation. Mice were then returned to the dam.

### *Statistical Analysis*

One-way ANOVA was used to compare the vascular and oxygen-metabolic changes in the normothermia *vs.* hypothermia experiment (***Figure 1E***), and to assess mitochondrial function in the UN, CL, and IL cortices (***Figure 2F–H***). Student t-test was used to compare the hemodynamic and oxygen-metabolic changes in the normoxia *vs.* hypoxia experiment (***Figure 1G***), and the infarct volume of normothermia or hypothermia (***Figure 4D***). Two-way ANOVA was used to compare the oxygen-metabolic changes of the CL and IL cortices in the Vannucci HI model under normothermic (***Figure 2B–D***) or hypothermic (***Figure 3B–E***) condition, the mitochondrial function (***Figure 3F–I***) and ATP level (***Figure 3J***) of CL or IL cortices under hypothermia, and the hemodynamic and oxygen-metabolic changes 24 hours post-HI (***Figure 4E–I***). All data were presented in the form of mean ± standard deviation of the mean. In all statistical analyses, $p < 0.05$ was considered significant.


## Acknowledgments

We thank Dr. Vadim Ten for demonstrating the mitochondria isolation and analysis methods.


## Additional files

***Supplementary files:*** **Figure S1.** Relationship between the water tank temperature and the mouse skull temperature. **Figure S2.** Oxygen consumption of mitochondria isolated from the uninjured (UN), contralateral (CL), and ipsilateral (IL) cortex at (A) 2 hours or (B) 5 hours post-HI. **Figure S3.** $^{1}$H-HRMAS MRS analysis of the effects of normothermia *vs.* hypothermia on brain metabolites at 24 hours post-HI. **Figure S4.** Potential mechanisms that contribute to the uncoupling of OXPHOS after HI and the effects of therapeutic hypothermia. **Table S1.** CBF, OEF, and $CMRO_2$ values measured at 37 °C in the contralateral (green) and ipsilateral (red) cortex in the indicated period that correspond to those illustrated in *Figure 2A*. **Table S2.** CBF, OEF, and $CMRO_2$ values with post-HI hypothermia treatment, measured at 32 °C in the contralateral (green) and ipsilateral (red) cortex in the indicated period that correspond to those illustrated in *Figure 3A*.

## References


Allen KA, Brandon DH. 2011. Hypoxic Ischemic Encephalopathy: Pathophysiology and Experimental Treatments. *Newborn Infant Nurs Rev* **11**:125–133. doi:10.1053/j.nainr.2011.07.004

Altman DI, Perlman JM, Volpe JJ, Powers WJ. 1993. Cerebral oxygen metabolism in newborns. *Pediatrics* **92**:99–104.

Benzi RH, Lerch R. 1992. Dissociation between contractile function and oxidative metabolism in postischemic myocardium. Attenuation by ruthenium red administered during reperfusion. *Circ Res* **71**:567–576. doi:10.1161/01.res.71.3.567

Berntman L, Welsh FA, Harp JR. 1981. Cerebral protective effect of low-grade hypothermia. *Anesthesiology* **55**:495–498. doi:10.1097/00000542-198111000-00003

Blumberg RM, Cady EB, Wigglesworth JS, McKenzie JE, Edwards AD. 1997. Relation between delayed impairment of cerebral energy metabolism and infarction following transient focal hypoxia-ischaemia in the developing brain. *Exp Brain Res* **113**:130–137. doi:10.1007/BF02454148

Buckley EM, Patel SD, Miller BF, Franceschini MA, Vannucci SJ. 2015. In vivo Monitoring of Cerebral Hemodynamics in the Immature Rat: Effects of Hypoxia-Ischemia and Hypothermia. *Dev Neurosci* **37**:407–416. doi:10.1159/000381704

Burnsed J, Skwarzyńska D, Wagley PK, Isbell L, Kapur J. 2019. Neuronal Circuit Activity during Neonatal Hypoxic-Ischemic Seizures in Mice. *Ann Neurol* **86**:927–938. doi:10.1002/ana.25601

Cao R, Li J, Ning B, Sun N, Wang T, Zuo Z, Hu S. 2017. Functional and oxygen-metabolic photoacoustic microscopy of the awake mouse brain. *NeuroImage* **150**:77–87. doi:10.1016/j.neuroimage.2017.01.049

Caspersen CS, Sosunov A, Utkina-Sosunova I, Ratner VI, Starkov AA, Ten VS. 2008. An isolation method for assessment of brain mitochondria function in neonatal mice with hypoxic-ischemic brain injury. *Dev Neurosci* **30**:319–324. doi:10.1159/000121416

Chen H-R, DeGrauw T, Kuan C-Y. 2022. (Phospho)creatine: the reserve and merry-go-round of brain energetics. *Neural Regen Res* **18**:327–328. doi:10.4103/1673-5374.346470

Chen H-R, Zhang-Brotzge X, Morozov YM, Li Y, Wang S, Zhang HH, Kuan IS, Fugate EM, Mao H, Sun Y-Y, Rakic P, Lindquist DM, DeGrauw T, Kuan C-Y. 2021. Creatine transporter deficiency impairs stress adaptation and brain energetics homeostasis. *JCI Insight* **6**:140173. doi:10.1172/jci.insight.140173

Cooper CE, Giulivi C. 2007. Nitric oxide regulation of mitochondrial oxygen consumption II: Molecular mechanism and tissue physiology. *Am J Physiol Cell Physiol* **292**:C1993-2003. doi:10.1152/ajpcell.00310.2006

De Carli A, Andresen B, Giovannella M, Durduran T, Contini D, Spinelli L, Weigel UM, Passera S, Pesenti N, Mosca F, Torricelli A, Fumagalli M, Greisen G. 2019. Cerebral oxygenation and blood flow in term infants during postnatal transition: BabyLux project. *Arch Dis Child Fetal Neonatal Ed* **104**:F648–F653. doi:10.1136/archdischild-2018-316400

Dehaes M, Aggarwal A, Lin P-Y, Rosa Fortuno C, Fenoglio A, Roche-Labarbe N, Soul JS, Franceschini MA, Grant PE. 2014. Cerebral oxygen metabolism in neonatal hypoxic ischemic encephalopathy during and after therapeutic hypothermia. *J Cereb Blood Flow Metab* **34**:87–94. doi:10.1038/jcbfm.2013.165

Erecinska M, Thoresen M, Silver IA. 2003. Effects of hypothermia on energy metabolism in Mammalian central nervous system. *J Cereb Blood Flow Metab* **23**:513–530. doi:10.1097/01.WCB.0000066287.21705.21

Ferradal SL, Yuki K, Vyas R, Ha CG, Yi F, Stopp C, Wypij D, Cheng HH, Newburger JW, Kaza AK, Franceschini MA, Kussman BD, Grant PE. 2017. Non-invasive Assessment of Cerebral Blood Flow and Oxygen Metabolism in Neonates during Hypothermic Cardiopulmonary Bypass: Feasibility and Clinical Implications. *Sci Rep* **7**:44117. doi:10.1038/srep44117

Fox PT, Raichle ME. 1986. Focal physiological uncoupling of cerebral blood flow and oxidative metabolism during somatosensory stimulation in human subjects. *Proc Natl Acad Sci U S A* **83**:1140–1144. doi:10.1073/pnas.83.4.1140

Gao Y-R, Ma Y, Zhang Q, Winder AT, Liang Z, Antinori L, Drew PJ, Zhang N. 2017. Time to wake up: Studying neurovascular coupling and brain-wide circuit function in the un-anesthetized animal. *Neuroimage* **153**:382–398. doi:10.1016/j.neuroimage.2016.11.069

Granger DN, Kvietys PR. 2015. Reperfusion injury and reactive oxygen species: The evolution of a concept. *Redox Biol* **6**:524–551. doi:10.1016/j.redox.2015.08.020

Grant PE, Roche-Labarbe N, Surova A, Themelis G, Selb J, Warren EK, Krishnamoorthy KS, Boas DA, Franceschini MA. 2009. Increased cerebral blood volume and oxygen consumption in neonatal brain injury. *J Cereb Blood Flow Metab* **29**:1704–1713. doi:10.1038/jcbfm.2009.90

Gunn AJ, Gunn TR, de Haan HH, Williams CE, Gluckman PD. 1997. Dramatic neuronal rescue with prolonged selective head cooling after ischemia in fetal lambs. *J Clin Invest* **99**:248–256.

Gunn AJ, Laptook AR, Robertson NJ, Barks JD, Thoresen M, Wassink G, Bennet L. 2017. Therapeutic hypothermia translates from ancient history in to practice. *Pediatr Res* **81**:202–209. doi:10.1038/pr.2016.198

Hägerdal M, Harp J, Siesjö BK. 1975. Effect of hypothermia upon organic phosphates, glycolytic metabolites, citric acid cycle intermediates and associated amino acids in rat cerebral cortex. *J Neurochem* **24**:743–748.

Jain V, Buckley EM, Licht DJ, Lynch JM, Schwab PJ, Naim MY, Lavin NA, Nicolson SC, Montenegro LM, Yodh AG, Wehrli FW. 2014. Cerebral oxygen metabolism in neonates with congenital heart disease quantified by MRI and optics. *J Cereb Blood Flow Metab* **34**:380–388. doi:10.1038/jcbfm.2013.214

Jespersen SN, Østergaard L. 2012. The roles of cerebral blood flow, capillary transit time heterogeneity, and oxygen tension in brain oxygenation and metabolism. *J Cereb Blood Flow Metab* **32**:264–277. doi:10.1038/jcbfm.2011.153

Juhaszova M, Zorov DB, Kim S-H, Pepe S, Fu Q, Fishbein KW, Ziman BD, Wang S, Ytrehus K, Antos CL, Olson EN, Sollott SJ. 2004. Glycogen synthase kinase-3beta mediates convergence of protection signaling to inhibit the mitochondrial permeability transition pore. *J Clin Invest* **113**:1535–1549. doi:10.1172/JCI19906

Khacho M, Tarabay M, Patten D, Khacho P, MacLaurin JG, Guadagno J, Bergeron R, Cregan SP, Harper M-E, Park DS, Slack RS. 2014. Acidosis overrides oxygen deprivation to maintain mitochondrial function and cell survival. *Nat Commun* **5**:3550. doi:10.1038/ncomms4550

Kim M, Stepanova A, Niatsetskaya Z, Sosunov S, Arndt S, Murphy MP, Galkin A, Ten VS. 2018. Attenuation of oxidative damage by targeting mitochondrial complex I in neonatal hypoxic-ischemic brain injury. *Free Radic Biol Med* **124**:517–524. doi:10.1016/j.freeradbiomed.2018.06.040

Kramer RS, Pearlstein RD. 1983. Reversible uncoupling of oxidative phosphorylation at low oxygen tension. *Proc Natl Acad Sci U S A* **80**:5807–5811. doi:10.1073/pnas.80.19.5807

Kristián T, Siesjö BK. 1998. Calcium in ischemic cell death. *Stroke* **29**:705–718. doi:10.1161/01.str.29.3.705

Kuan C-Y, Chen H-R, Gao N, Kuo Y-M, Chen C-W, Yang D, Kinkaid MM, Hu E, Sun Y-Y. 2021. Brain-targeted hypoxia-inducible factor stabilization reduces neonatal hypoxic-ischemic brain injury. *Neurobiol Dis* **148**:105200. doi:10.1016/j.nbd.2020.105200

Lee J-M, Vo KD, An H, Celik A, Lee Y, Hsu CY, Lin W. 2003. Magnetic resonance cerebral metabolic rate of oxygen utilization in hyperacute stroke patients. *Ann Neurol* **53**:227–232. doi:10.1002/ana.10433

Lin W, Powers WJ. 2018. Oxygen metabolism in acute ischemic stroke. *J Cereb Blood Flow Metab* **38**:1481–1499. doi:10.1177/0271678X17722095

Liu P, Chalak LF, Lu H. 2014a. Non-invasive Assessment of Neonatal Brain Oxygen Metabolism: A Review of Newly Available Techniques. *Early Hum Dev* **90**:695–701. doi:10.1016/j.earlhumdev.2014.06.009

Liu P, Huang H, Rollins N, Chalak LF, Jeon T, Halovanic C, Lu H. 2014b. Quantitative assessment of global cerebral metabolic rate of oxygen (CMRO2) in neonates using MRI. *NMR Biomed* **27**:332–340. doi:10.1002/nbm.3067

Murphy MP. 2009. How mitochondria produce reactive oxygen species. *Biochem J* **417**:1–13. doi:10.1042/BJ20081386

Niatsetskaya ZV, Sosunov SA, Matsiukevich D, Utkina-Sosunova IV, Ratner VI, Starkov AA, Ten VS. 2012. The oxygen free radicals originating from mitochondrial complex I contribute to oxidative brain injury following hypoxia-ischemia in neonatal mice. *J Neurosci* **32**:3235–3244. doi:10.1523/JNEUROSCI.6303-11.2012

Paradies G, Paradies V, Ruggiero FM, Petrosillo G. 2018. Mitochondrial bioenergetics and cardiolipin alterations in myocardial ischemia-reperfusion injury: implications for pharmacological cardioprotection. *Am J Physiol Heart Circ Physiol* **315**:H1341–H1352. doi:10.1152/ajpheart.00028.2018

Paulson OB, Hasselbalch SG, Rostrup E, Knudsen GM, Pelligrino D. 2010. Cerebral blood flow response to functional activation. *J Cereb Blood Flow Metab* **30**:2–14. doi:10.1038/jcbfm.2009.188

Piilgaard H, Lauritzen M. 2009. Persistent increase in oxygen consumption and impaired neurovascular coupling after spreading depression in rat neocortex. *J Cereb Blood Flow Metab* **29**:1517–1527. doi:10.1038/jcbfm.2009.73

Rolfe DF, Brown GC. 1997. Cellular energy utilization and molecular origin of standard metabolic rate in mammals. *Physiological Reviews* **77**:731–758. doi:10.1152/physrev.1997.77.3.731

Salford LG, Siesjö BK. 1974. The influence of arterial hypoxia and unilateral carotid artery occlusion upon regional blood flow and metabolism in the rat brain. *Acta Physiol Scand* **92**:130–141. doi:10.1111/j.1748-1716.1974.tb05729.x

Sciortino VM, Tran A, Sun N, Cao R, Sun T, Sun Y-Y, Yan P, Zhong F, Zhou Y, Kuan C-Y, Lee J-M, Hu S. 2021. Longitudinal cortex-wide monitoring of cerebral hemodynamics and oxygen metabolism in awake mice using multi-parametric photoacoustic microscopy. *J Cereb Blood Flow Metab* **41**:3187–3199. doi:10.1177/0271678X211034096

Slupe AM, Kirsch JR. 2018. Effects of anesthesia on cerebral blood flow, metabolism, and neuroprotection. *J Cereb Blood Flow Metab* **38**:2192–2208. doi:10.1177/0271678X18789273

Starkov AA, Fiskum G. 2003. Regulation of brain mitochondrial H2O2 production by membrane potential and NAD(P)H redox state. *J Neurochem* **86**:1101–1107. doi:10.1046/j.1471-4159.2003.01908.x

Sun N, Ning B, Bruce AC, Cao R, Seaman SA, Wang T, Fritsche-Danielson R, Carlsson LG, Peirce SM, Hu S. 2020. In vivo imaging of hemodynamic redistribution and arteriogenesis across microvascular network. *Microcirculation* **27**:e12598. doi:10.1111/micc.12598

Thorngren-Jerneck K, Ohlsson T, Sandell A, Erlandsson K, Strand SE, Ryding E, Svenningsen NW. 2001. Cerebral glucose metabolism measured by positron emission tomography in term newborn infants with hypoxic ischemic encephalopathy. *Pediatr Res* **49**:495–501. doi:10.1203/00006450-200104000-00010

Tsuji M, Naruse H, Volpe J, Holtzman D. 1995. Reduction of cytochrome aa3 measured by near-infrared spectroscopy predicts cerebral energy loss in hypoxic piglets. *Pediatr Res* **37**:253–259. doi:10.1203/00006450-199503000-00001

Vestergaard MB, Lindberg U, Aachmann-Andersen NJ, Lisbjerg K, Christensen SJ, Law I, Rasmussen P, Olsen NV, Larsson HBW. 2016. Acute hypoxia increases the cerebral metabolic rate - a magnetic resonance imaging study. *J Cereb Blood Flow Metab* **36**:1046–1058. doi:10.1177/0271678X15606460

Yager JY, Brucklacher RM, Vannucci RC. 1992. Cerebral energy metabolism during hypoxia-ischemia and early recovery in immature rats. *Am J Physiol* **262**:H672-677. doi:10.1152/ajpheart.1992.262.3.H672

Yang D, Nemkul N, Shereen A, Jone A, Dunn RS, Lawrence DA, Lindquist D, Kuan C-Y. 2009. Therapeutic administration of plasminogen activator inhibitor-1 prevents hypoxic-ischemic brain injury in newborns. *J Neurosci* **29**:8669–8674. doi:10.1523/JNEUROSCI.1117-09.2009

## Figures and figure legends

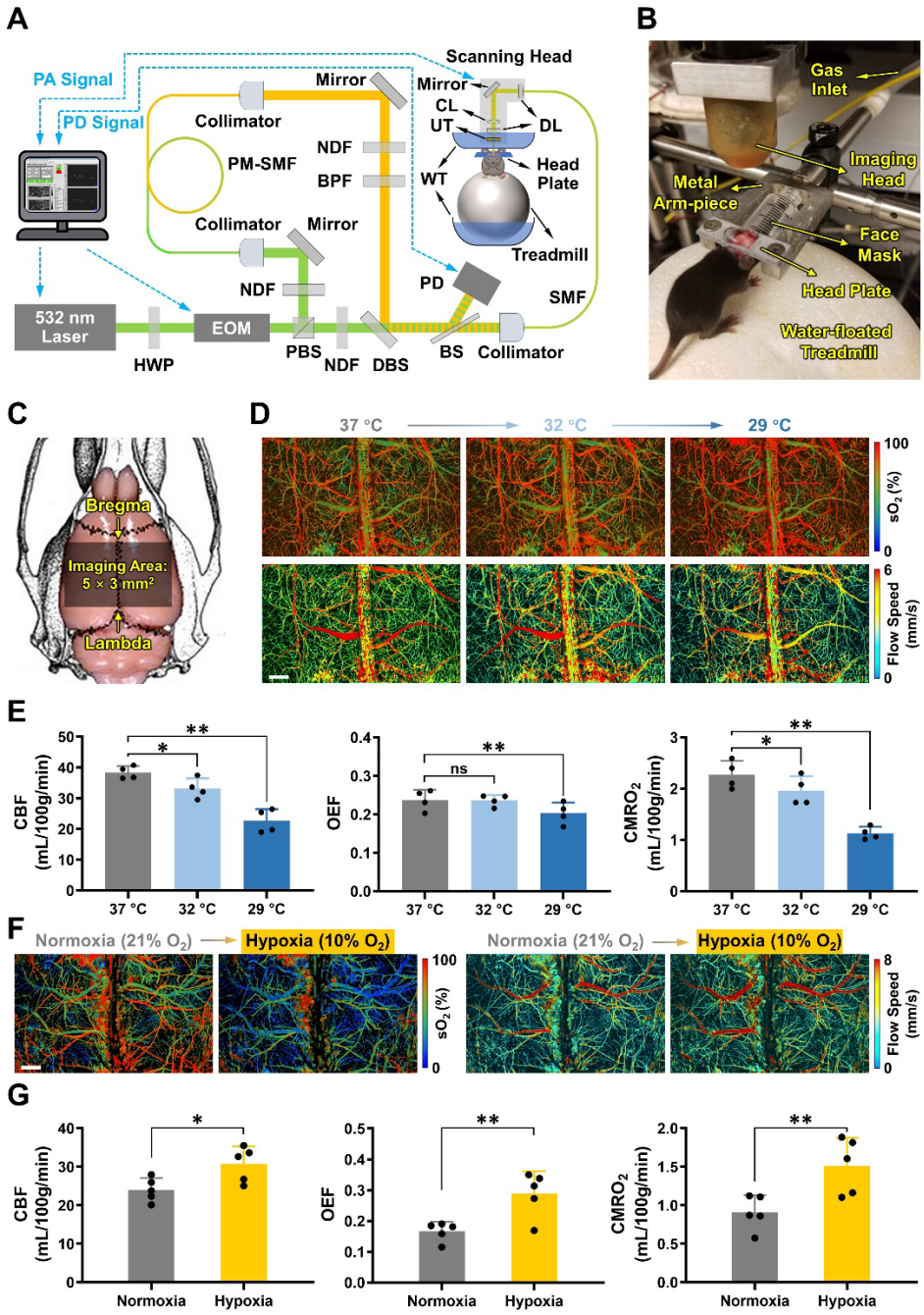


**Figure 1. Multi-parametric photoacoustic microscopy (PAM) of hemodynamic and oxygen-metabolic responses of uninjured neonatal mouse brains to hypothermia or hypoxia**. (**A**) Schematic of the head-restrained multi-parametric PAM system. PA, photoacoustic; PD, photodiode; HWP, half-wave plate; EOM, electro-optical modulator; PBS, polarizing beam splitter; NDF, neutral-density filter; PM-SMF, polarization-maintaining single-mode fiber; BPF,

band-pass filter; DBS, dichroic beam splitter; BS, beam sampler; SMF, single-mode fiber; DL, doublet; CL, correction lens; UT, ring-shaped ultrasonic transducer; WT, water tank. (**B**) Photograph of the placement of an awake 10-day-old (P10) mouse wearing the head plate in the PAM system. Note that the water tank is removed to better show the mouse and related parts for head-restrained awake-brain imaging. (**C**) Illustration of the imaging field ($5 \times 3$ mm$^2$) that covers both hemicortices between the Bregma and Lambda on the skull of mouse neonates. (**D**) Multi-parametric PAM images of the oxygen saturation of hemoglobin ($sO_2$) and blood flow speed in an awake P10 mouse, with the skull temperature set at 37, 32, and 29 °C, respectively. Scale bar: 500 μm. (**E**) Hemodynamic and oxygen-metabolic responses of the neonatal mouse cortex to different skull temperatures, including cerebral blood flow (CBF), oxygen extraction fraction (OEF), and the cerebral metabolic rate of oxygen ($CMRO_2$). Gray bars: 37 °C; light blue bars: 32 °C; dark blue bars: 29 °C. One-way ANOVA was performed, and data are presented as mean ± standard deviation (n = 4). ns, no significance; *, $p < 0.05$; **, $p < 0.01$. (**F**) Multi-parametric PAM images of $sO_2$ and blood flow speed in an anesthetized P10 mouse under normoxia (inhaled oxygen concentration: 21%) versus hypoxia (inhaled oxygen concentration: 10%). Scale bar: 500 μm. (**G**) Hemodynamic and oxygen-metabolic responses of the neonatal mouse cortex to normoxia *vs.* hypoxia, including CBF, OEF, and $CMRO_2$. Gray bars: normoxia; orange bars: hypoxia. Student t-test was performed, and data are presented as mean ± standard deviation (n = 5). *, $p < 0.05$; **, $p < 0.01$.

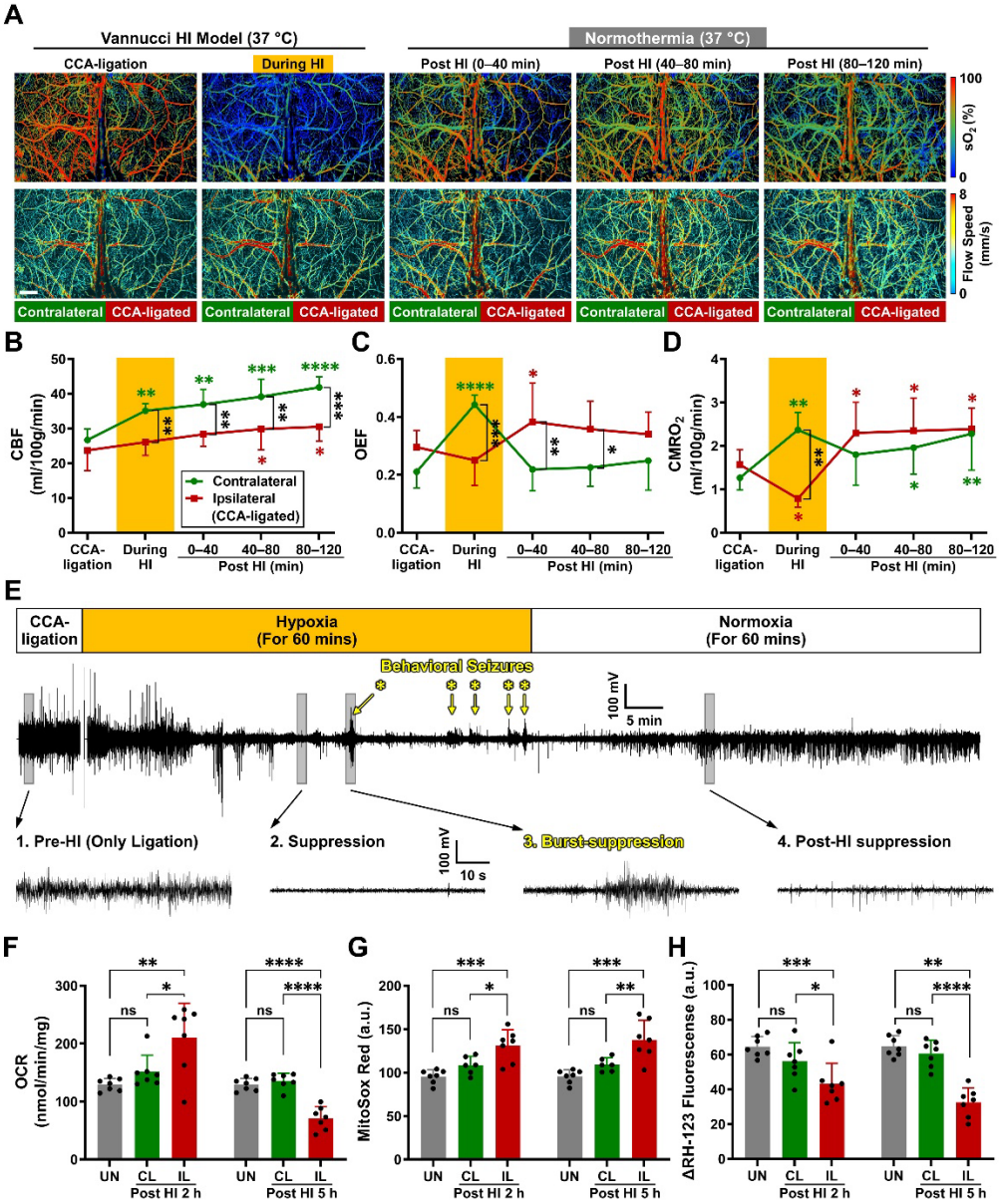


**Figure 2. Effects of combined hypoxia-ischemia (HI) on cerebral hemodynamics, oxygen metabolism, and mitochondrial bioenergetics in mouse neonates under normothermia.** (**A**) Time-lapse PAM images of the oxygen saturation of hemoglobin ($sO_2$) and blood flow speed in an awake P10 mouse during unilateral CCA-ligation, combined HI, as well as 0–40, 40–80, and 80–120 minutes post-HI. Scale bar: 500 µm. (**B–D**) Hemodynamic and oxygen-metabolic responses of the contralateral (green line and symbols) and ipsilateral (red line and symbols) cortices to the Vannucci HI Model under normothermia, including (**B**) cerebral blood flow (CBF), (**C**) oxygen extraction fraction (OEF), and (**D**) the cerebral metabolic rate of oxygen

($CMRO_2$). Green and red asterisks indicate the statistical significance, if any, over the baseline (i.e., CCA-ligation alone) values measured in the same animal, while black asterisks indicate the statistical significance, if any, between the measurements in the two hemicortices at the same time point. Two-way ANOVA was performed, and data are presented as mean ± standard deviation (n = 5). *, $p < 0.05$; **, $p < 0.01$; ***, $p < 0.001$; ****, $p < 0.0001$. (**E**) Electroencephalography (EEG) recording of the ipsilateral cortex in a P10 mouse right after the unilateral CCA-ligation, 60-minute hypoxia (inhaled oxygen concentration: 10%), and 60-minute normoxia (inhaled oxygen concentration: 21%). Zoom-in views of the boxed regions show characteristic EEG patterns, including 1. pre-HI baseline, 2. Suppression, 3. burst-suppression correlated with seizure behaviors (highlighted by yellow asterisks), and 4. post-HI suppression. n = 6. (**F–H**) Comparison of the mitochondrial parameters acquired in the uninjured (UN, gray bars), contralateral (CL, green bars), and ipsilateral (IL, red bars) cortices at 2 or 5 hours post-HI, including (**F**) oxygen consumption rate (OCR), (**G**) MitoSox Red, and (**H**) ΔRH-123 fluorescence. One-way ANOVA was performed, and data are presented as mean ± standard deviation (n = 7). ns, no significance; *, $p < 0.05$; **, $p < 0.01$; ***, $p < 0.001$; ****, $p < 0.0001$.

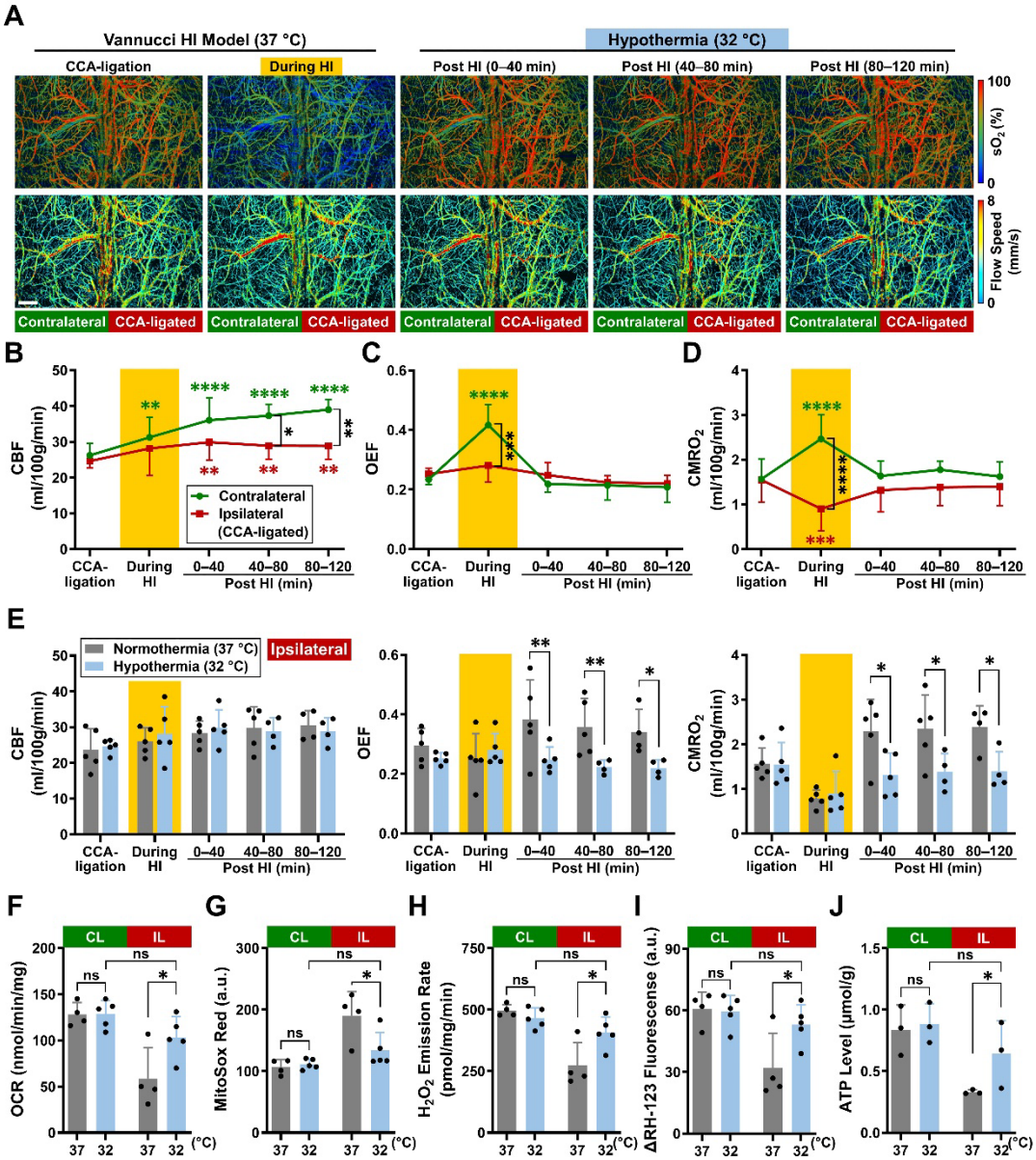


**Figure 3. Effects of hypoxia-ischemia (HI) on cerebral hemodynamics, oxygen metabolism, and mitochondrial bioenergetics in mouse neonates under hypothermia *vs.* normothermia.** (**A**) Time-lapse PAM images of the oxygen saturation of hemoglobin ($sO_2$) and blood flow speed in an awake P10 mouse during unilateral CCA-ligation, combined HI, as well as 0–40, 40–80, and 80–120 minutes post-HI. Scale bar: 500 μm. (**B–D**) Hemodynamic and oxygen-metabolic responses of the contralateral (green line and symbols) and ipsilateral (red line and symbols) cortices to the Vannucci HI Model under hypothermia, including (**B**) cerebral blood flow (CBF), (**C**) oxygen extraction fraction (OEF), and (**D**) the cerebral metabolic rate of oxygen ($CMRO_2$). Green and red asterisks indicate the statistical significance, if any, over the baseline (i.e., CCA-

ligation alone) values measured in the same animal, while black asterisks indicate the statistical significance, if any, between the measurements in the two hemicortices at the same time point. (**E**) Comparison of CBF, OEF, and $CMRO_2$ responses of the ipsilateral cortex to the HI insult under normothermia (37 °C, gray bars) *vs* hypothermia (32 °C, light blue bars). For (**B–E**), two-way ANOVA was performed, and data are presented as mean ± standard deviation (n = 5). *, $p < 0.05$; **, $p < 0.01$; ***, $p < 0.001$; ****, $p < 0.0001$. (*F–I*) Comparison of the mitochondrial parameters acquired in the contralateral (CL, green bars) and ipsilateral (IL, red bars) cortices at 5 hours post-HI under normothermia (37 °C, gray bars) *vs* hypothermia (32 °C, light blue bars), including (**F**) oxygen consumption rate (OCR), (**G**) MitoSox Red, (**H**) $H_2O_2$ emission rate, and (*I*) ΔRH-123 fluorescence. Two-way ANOVA was performed, and data are presented as mean ± standard deviation (n = 4 or 5 for normothermia or hypothermia treatment group, respectively). ns, no significance; *, $p < 0.05$. (*J*) Comparison of the ATP concentrations measured in the CL and IL cortices at 6 hours post-HI under normothermia (37 °C, gray bars) *vs* hypothermia (32 °C, light blue bars). Two-way ANOVA was performed, and data are presented as mean ± standard deviation (n = 3). ns, no significance; *, $p < 0.05$. For (**F–J**), the *in-vitro* analyses were performed in mitochondria isolated from HI-injured mice with or without a 4-hour hypothermia treatment, followed by another (**F–I**) one hour or (**J**) two hours recovery in normothermia.

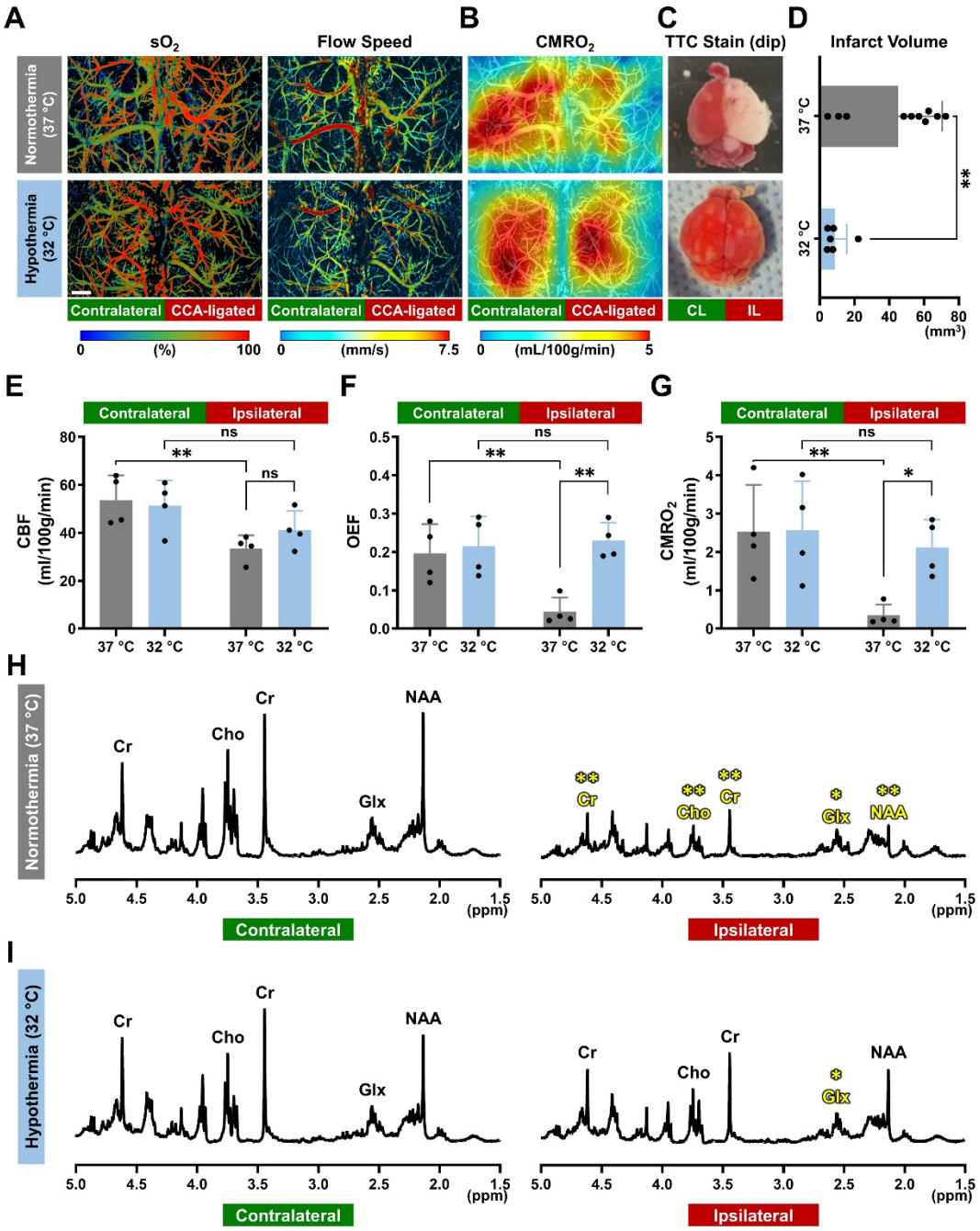


**Figure 4. Correlation of $CMRO_2$ and post-HI brain infarction in mouse neonates.** (**A–C**) Multi-parametric PAM images of (**A**) the oxygen saturation of hemoglobin ($sO_2$) and blood flow speed and (**B**) the cerebral metabolic rate of oxygen ($CMRO_2$), as well as (**C**) the triphenyl-tetrazolium chloride (TTC) analysis of the dissected brain after completion of the *in vivo* PAM imaging at 24 hours post-HI. The top and bottom rows are data acquired in the neonate brain treated with normothermia (37 °C, upper row) or hypothermia (32 °C, lower row) for 4 hours, respectively. CL, contralateral; IL, ipsilateral. Scale bar: 500 µm. (**D**) Comparison of the infarct

volume quantified based on the TTC analysis (n = 6 for the normothermia group and n = 10 for the hypothermia group). Student *t*-test was performed, and data are presented as mean ± standard deviation. **, $p < 0.01$. (**E–G**) Comparison of (**E**) cerebral blood flow (CBF), (**F**) oxygen extraction fraction (OEF), and (**G**) $CMRO_2$ acquired at 24 hours post-HI in the neonate brain treated with normothermia (37 °C, gray bars) or hypothermia (32 °C, light blue bars) for 4 hours. Two-way ANOVA was performed, and data are presented as mean ± standard deviation (n = 4). ns, no significance; *, $p < 0.05$; **, $p < 0.01$. (**H–I**) Characteristic proton-HRMAS spectra of the snap-frozen tissue from the contralateral and ipsilateral cortex extracted at 24 hours post-HI from HI-injured mice treated with (**H**) normothermia or (**I**) hypothermia. The spectra are scaled to the same peak height for myo-inositol. Cr, creatine and phosphocreatine; Cho, choline; Glx, glutamate and glutamine; NAA, N-acetyl aspartate. Two-way ANOVA was performed (n = 5 for normothermia and n = 3 for hypothermia). *, $p < 0.05$; **, $p < 0.01$.

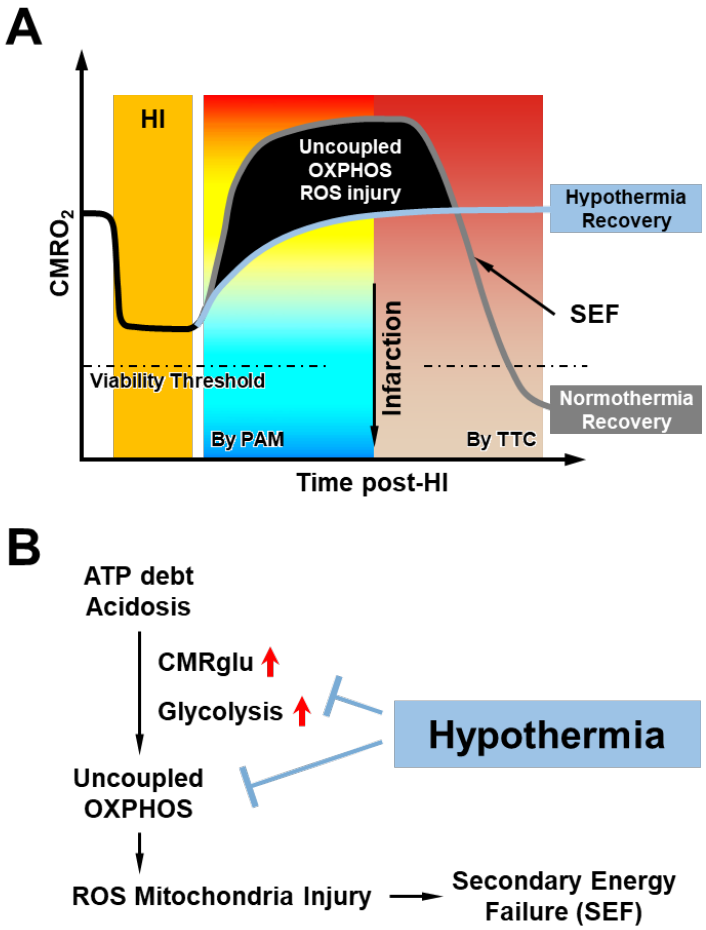


**Figure 5. Schematic conclusion and open questions.** (**A**) Combined hypoxia-ischemia (HI) initially suppresses cerebral oxygen metabolism, but sparks a rapid rebound and overshoot of post-HI $CMRO_2$ caused by uncoupled OXPHOS with greater ROS emission, which leads to the demise of mitochondria and the onset of secondary energy failure (SEF). In contrast, recovery at hypothermia attenuates the post-HI surge of mitochondrial respiration and produces more enduring cerebral oxygen metabolism. The threshold of $CMRO_2$-reduction that causes brain infarction in neonates is expected to exist but yet to be established. (**B**) The combination of energy deficit and tissue acidosis accumulated during HI plus increased glucose-uptake and glycolysis acutely after HI stimulates uncoupled OPXHOS in the HI-injured neonatal brain, leading to excessive ROS emission and rapid mitochondrial injury. According to the literature (Berntman et al., 1981; Hägerdal et al., 1975) and our results, hypothermia may interrupt this pathological process by inhibiting glycolysis and the TCA cycle.

Supplementary files

# Dual-modal metabolic analysis reveals hypothermia-reversible uncoupling of oxidative phosphorylation in neonatal brain hypoxia-ischemia

*Naidi Sun, Yu-Yo Sun, Rui Cao, Hong-Ru Chen, Yiming Wang, Elizabeth Fugate, Marchelle R. Smucker, Yi-Min Kuo, P. Ellen Grant, Diana M. Lindquist, Chia-Yi Kuan*, and Song Hu**

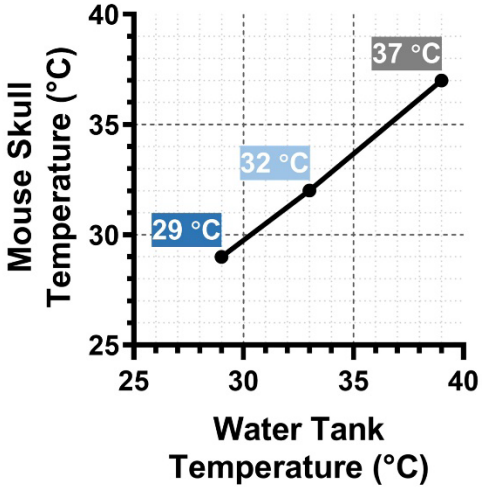


**Figure S1.** Relationship between the water tank temperature and the mouse skull temperature.

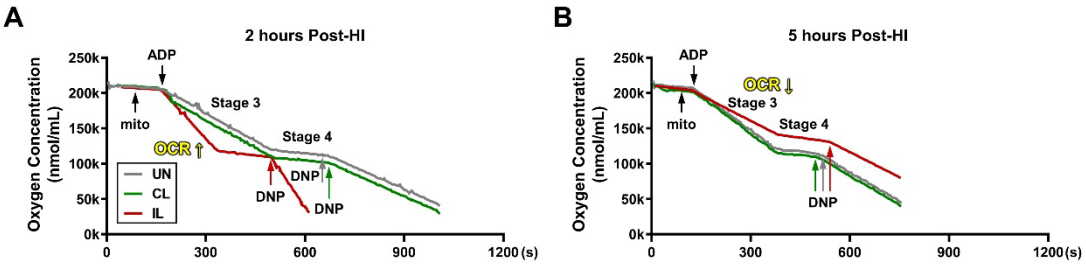


**Figure S2.** Oxygen consumption of mitochondria isolated from the uninjured (UN), contralateral (CL), and ipsilateral (IL) cortex at (*A*) 2 hours or (*B*) 5 hours post-HI. HI, hypoxia-ischemia; mito, mitochondria protein; ADP, adenosine diphosphate; DNP, 2'- 4' Dinitrophenol; OCR, oxygen consumption rate.

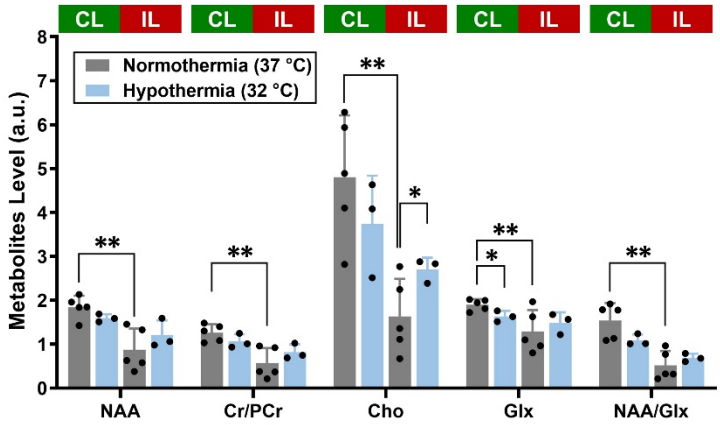


**Figure S3.** $^{1}$H-HRMAS MRS analysis of the effects of normothermia *vs.* hypothermia on brain metabolites at 24 hours post-HI. NAA, N-acetyl aspartate; Cr, creatine; PCr, phosphocreatine; Cho, choline; Glx, glutamate. Two-way ANOVA was performed (n = 5 for normothermia and n = 3 for hypothermia). *, $p < 0.05$; **, $p < 0.01$.

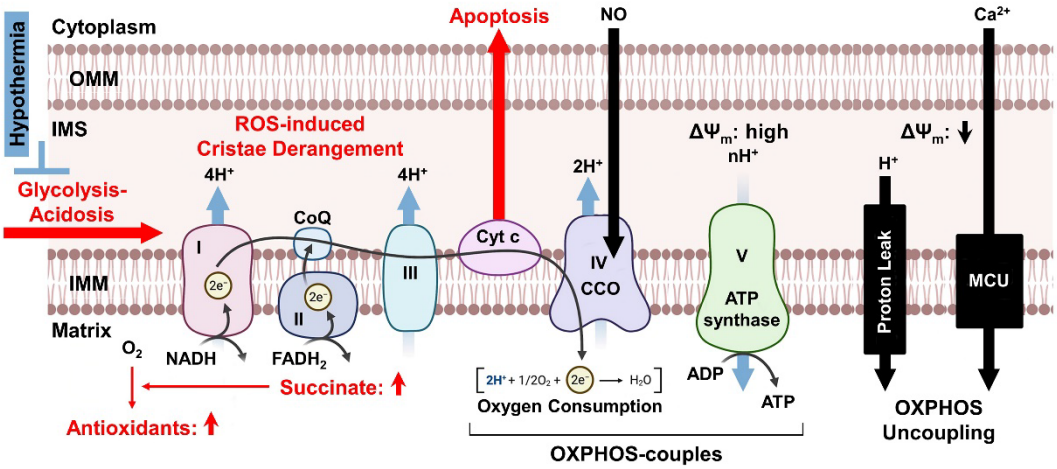


**Figure S4.** Potential mechanisms that contribute to the uncoupling of OXPHOS after HI and the effects of therapeutic hypothermia. OMM, outer mitochondrial membrane; IMM, inner mitochondrial membrane; IMS, mitochondrial intermembrane space; ROS, reactive oxygen species; NADH, nicotinamide adenine dinucleotide hydrogen; $FADH_2$, flavin adenine dinucleotide; CoQ, Coenzyme Q; cyt c, cytochrome complex; NO, nitric oxide; CCO, cytochrome c oxidase; $\Delta\Psi_m$, mitochondrial membrane potential; MCU, mitochondrial calcium uniporter; OXPHOS, oxidative phosphorylation.

**Table S1.** CBF, OEF, and $CMRO_2$ values measured at 37 °C in the contralateral (green) and ipsilateral (red) cortex in the indicated period that correspond to those illustrated in Fig. 2*A*. Data are shown in mean ± SD and compared to the "CCA-ligation" on its own side, unless indicated with a bracket. The *p*-values were determined by two-way ANOVA (n=5; *: p<0.05; **: p<0.01).

| Normothermia (37 °C) | Contralateral (CL) Hemisphere | | | |
|---|---|---|---|---|
| | CBF (mL/100g/min) | OEF | $CMRO_2$ (mL/100g/min) | |
| CCA-ligation | 26.672 ± 2.863 | 0.210 ± 0.050 | 1.261 ± 0.252 | |
| Hypoxia-Ischemia | 35.107 ± 1.865 | 0.442 ± 0.029 | 2.366 ± 0.355 ** | |
| Post-HI (0–40 mins) | 36.916 ± 3.879 | 0.218 ± 0.066 | 1.797 ± 0.628 | |
| Post-HI (40–80 mins) | 39.143 ± 4.532 | 0.225 ± 0.058 | 1.956 ± 0.545 * | ** |
| Post-HI (80–120 mins) | 41.851 ± 2.638 | 0.249 ± 0.088 | 2.276 ± 0.726 ** | |
| | | | | |
| Normothermia (37 °C) | Ipsilateral (CL) Hemisphere | | | |
| | CBF (mL/100g/min) | OEF | $CMRO_2$ (mL/100g/min) | |
| CCA-ligation | 23.674 ± 5.205 | 0.295 ± 0.052 | 1.564 ± 0.313 | |
| Hypoxia-Ischemia | 26.034 ± 3.428 | 0.250 ± 0.077 | 0.782 ± 0.178 * | |
| Post-HI (0–40 mins) | 28.306 ± 3.096 | 0.383 ± 0.119 | 2.295 ± 0.632 * | |
| Post-HI (40–80 mins) | 29.787 ± 5.315 | 0.357 ± 0.086 | 2.342 ± 0.677 * | |
| Post-HI (80–120 mins) | 30.479 ± 3.593 | 0.340 ± 0.066 | 2.385 ± 0.416 * | |

**Table S2.** CBF, OEF, and $CMRO_2$ values with post-HI hypothermia treatment, measured at 32 °C in the contralateral (green) and ipsilateral (red) cortex in the indicated period that correspond to those illustrated in Fig. 3*A*. Data are shown in mean ± SD and compared to the "CCA-ligation" on its own side, unless indicated with a bracket. The *p*-values were determined by two-way ANOVA (n=5; ***: p<0.001; ****: p<0.0001).

| Hypothermia (32 °C) | Contralateral (CL) Hemisphere | | |
|---|---|---|---|
| | CBF (mL/100g/min) | OEF | $CMRO_2$ (mL/100g/min) |
| CCA-ligation | 26.184 ± 3.059 | 0.234 ± 0.015 | 1.563 ± 0.405 |
| Hypoxia-Ischemia | 31.234 ± 4.959 | 0.416 ± 0.061 | 2.464 ± 0.488 **** |
| Post-HI (0–40 mins) | 36.059 ± 5.635 | 0.218 ± 0.024 | 1.635 ± 0.298 |
| Post-HI (40–80 mins) | 37.324 ± 2.751 | 0.214 ± 0.043 | 1.776 ± 0.162 |
| Post-HI (80–120 mins) | 38.972 ± 2.501 | 0.208 ± 0.045 | 1.623 ± 0.289 |
| | | | |
| Hypothermia (32 °C) | Ipsilateral (CL) Hemisphere | | |
| | CBF (mL/100g/min) | OEF | $CMRO_2$ (mL/100g/min) |
| CCA-ligation | 24.613 ± 1.747 | 0.252 ± 0.017 | 1.545 ± 0.440 |
| Hypoxia-Ischemia | 28.130 ± 6.775 | 0.281 ± 0.050 | 0.902 ± 0.439 *** |
| Post-HI (0–40 mins) | 29.886 ± 4.456 | 0.248 ± 0.038 | 1.318 ± 0.435 |
| Post-HI (40–80 mins) | 28.902 ± 3.250 | 0.224 ± 0.019 | 1.379 ± 0.358 |
| Post-HI (80–120 mins) | 28.842 ± 3.223 | 0.220 ± 0.024 | 1.397 ± 0.375 |